Volume 18, Issue 3, 182448 (1-14)

Majlesi Journal of Electrical Engineering (MJEE)

https://dx.doi.org/10.57647/j.mjee.2024.180348

Artificial neural network sensorless direct torque control of two parallel-connected five-phase induction machines

Benzaoui Khaled Mohammed Said*, Benyoussef Elakhdar, Kouache Ahmed Zouhir

Faculté des Sciences Appliquées, Laboratoire LAGE, Université de Ouargla, Ouargla, Algeria.

*__Corresponding author:__ benzaoui.khaled@univ-ouargla.dz

Original Research

Received:
5 April 2024
Revised:
28 April 2024
Accepted:
15 July 2024
Published online:
3 September 2024

Abstract:

Conventional direct torque control (DTC) improves the dynamic performance of the five-phase induction machine (FPIM). Nevertheless, it suffers from significant drawbacks of high stator flux and electromagnetic torque ripples. Moreover, the DTC technique relies on an open-loop estimator for accurate stator flux module and position knowledge. However, this method is subjected to substandard performance, mainly during the low-speed operation range. Therefore, a sliding mode sensorless stator flux and rotor speed DTC based on an artificial neural network (DTC-ANN) for two parallel-connected FPIMs is discussed to tackle the problems above. This approach optimizes the DTC performance by replacing the two hysteresis controllers (HC) and the look-up table. As for the poor estimation drawback, the sliding mode observer (SMO) offers a robust estimation and reconstruction of the FPIM variables and eliminates the need for additional sensors, increasing the system's reliability. The present results verify and compare the performance of the control scheme.

Keywords: Five-phase induction motor (FPIM); Direct torque control (DTC); Artificial neural network (ANN); Parallel-connected two-motor drive; Sensorless control; Sliding mode observer (SMO)

1. Introduction

The multiphase induction machines are a promising solution for critical and high-power industrial applications. They retain the advantages of the well-known three-phase machines and additional features such as reduced current rating per phase. They are more adaptable for higher fault-tolerant applications [1–3]. Furthermore, the multiphase machines offer a higher torque density, lower torque pulsation, and better noise characteristics [3, 4].

Today, a wide range of applications have been proposed for this drive, namely Aerospace, marine, hybrid, and electric vehicle applications [3].

The five-phase induction machines FPIM have a growing interest in the literature because they offer a fair compromise between advantages of the multiphase machines, such as the additional degree of freedom DOF and complexity of the drive.

Given that the FPIM has additional DOFs, in other words, two sets of current components, and in response to the cost, weight, and compactness criterion, independent control of the two-motor parallel-connected drive fed by a single VSI is possible since the control of any AC machine requires only two current components under different working conditions (speed and load torque).

In the last point and from the control scheme point of view, the direct torque control scheme has garnered interest for its well-known excellent transient and steady-state performance. The DTC scheme selects the inverter voltage vectors VV based on the flux and torque HCs and the stator flux position based on a predefined look-up table; however, the conventional scheme results in considerable flux and torque ripples [5].

To overcome the drawbacks mentioned above, the research community proposed several improvements, including introducing artificial intelligence techniques, for instance, the artificial neural network ANN [6–8]. This control technique is known as an expert system and one of the most potent AI techniques in the field of electrical engineering for its ability to adapt to most operating conditions and its robustness to the system's nonlinearity [9–12].

Moreover, estimating the stator flux and torque is critical for DTC since these quantities determine the control scheme's performance. In the DTC, the method for estimating these variables is based on an open-loop estimator; nevertheless, this method is inefficient, especially in low-speed regions [13]. As a result, several sensorless control strategies are used in conjunction with DTC drives, such as the Extended Kalman Filter [14–16], Model reference adaptive system [17], and SMO [18–20]. These techniques have the advantages of reducing costs and increasing drive efficiency and reliability.

Therefore, the primary intention of this paper is to discuss a sensorless DTC-ANN based on SMO. The suggested method outperforms the conventional method regarding dynamic behavior.

The present paper consists of eight sections. Section 2 presents the model of the two motors. The basis of DTC for two motor drive is described in section 3. Section 4 discusses the combined DTC and ANN schemes for the drive. Section 5 presents a sliding-mode flux and speed observer. The load torque estimator is detailed in section 6. Simulation results and comparative study of the proposed two control techniques are given in section 7. Finally, the conclusion is reached in section 8.

2. The two FPIMS model

Figure 1 shows the two-motor parallel-connected drive schematics. The utilized converter topology is a two-level inverter. Table 1. describes the two possible switching functions for the inverter semiconductor switches constituting the 32 VV.

The inverter phase voltages are given as:

$$\begin{bmatrix} V_A \\ V_B \\ V_C \\ V_D \\ V_E \end{bmatrix} = \frac{V_{dc}}{5} \begin{bmatrix} 4 & -1 & -1 & -1 & -1 \\ -1 & 4 & -1 & -1 & -1 \\ -1 & -1 & 4 & -1 & -1 \\ -1 & -1 & -1 & 4 & -1 \\ -1 & -1 & -1 & -1 & 4 \end{bmatrix} \begin{bmatrix} S_A \\ S_B \\ S_C \\ S_D \\ S_E \end{bmatrix} \quad (1)$$

The voltage space vector decomposition of the inverter into β_1 and β_2 planes is given by:

$$\begin{cases} v_{\alpha\beta_1} = \frac{2}{5}\left(v_A + v_B e^{j\frac{2\pi}{5}} + v_C e^{j\frac{4\pi}{5}} + v_D e^{j\frac{6\pi}{5}} + v_E e^{j\frac{8\pi}{5}}\right) \\ v_{\alpha\beta_2} = \frac{2}{5}\left(v_A + v_C e^{j\frac{2\pi}{5}} + v_E e^{j\frac{4\pi}{5}} + v_B e^{j\frac{6\pi}{5}} + v_D e^{j\frac{8\pi}{5}}\right) \end{cases} \quad (2)$$

The 32 VV of the inverter mapping in and in figure 2 using Eq. (2).

These VVs are grouped into three types, i.e., large, medium, and small VVs, with amplitudes of $0.6472V_{dc}$, $0.4V_{dc}$, and $0.2{,}472V_{dc}$, respectively.

The five-dimensional system is decomposed, using Clark's transformation matrix $[C]$, into two orthogonal subspaces, $\alpha\beta_1$ and $\alpha\beta_2$, and zero sequence component [21]:

$$[C] = \frac{2}{5}\begin{bmatrix} 1 & \cos(\frac{2\pi}{5}) & \cos(\frac{4\pi}{5}) & \cos(\frac{6\pi}{5}) & \cos(\frac{8\pi}{5}) \\ 0 & \sin(\frac{2\pi}{5}) & \sin(\frac{4\pi}{5}) & \sin(\frac{6\pi}{5}) & \sin(\frac{8\pi}{5}) \\ 1 & \cos(\frac{4\pi}{5}) & \cos(\frac{8\pi}{5}) & \cos(\frac{2\pi}{5}) & \cos(\frac{6\pi}{5}) \\ 0 & \sin(\frac{4\pi}{5}) & \sin(\frac{8\pi}{5}) & \sin(\frac{2\pi}{5}) & \sin(\frac{6\pi}{5}) \\ \frac{1}{2} & \frac{1}{2} & \frac{1}{2} & \frac{1}{2} & \frac{1}{2} \end{bmatrix} \quad (3)$$

The two five-phase squirrel cage induction motors have five windings spatially shifted by 72 electrical degrees. As the motors are star-connected, the zero-sequence component is omitted. The two FPIMs model, in the stationary reference frame, under the same assumption as the three-phase motor

Table 1. Two-level inverter switching functions.

Switching function	State of the upper switch	The output voltage
1	On	V_{dc}
0	OFF	$-V_{dc}$

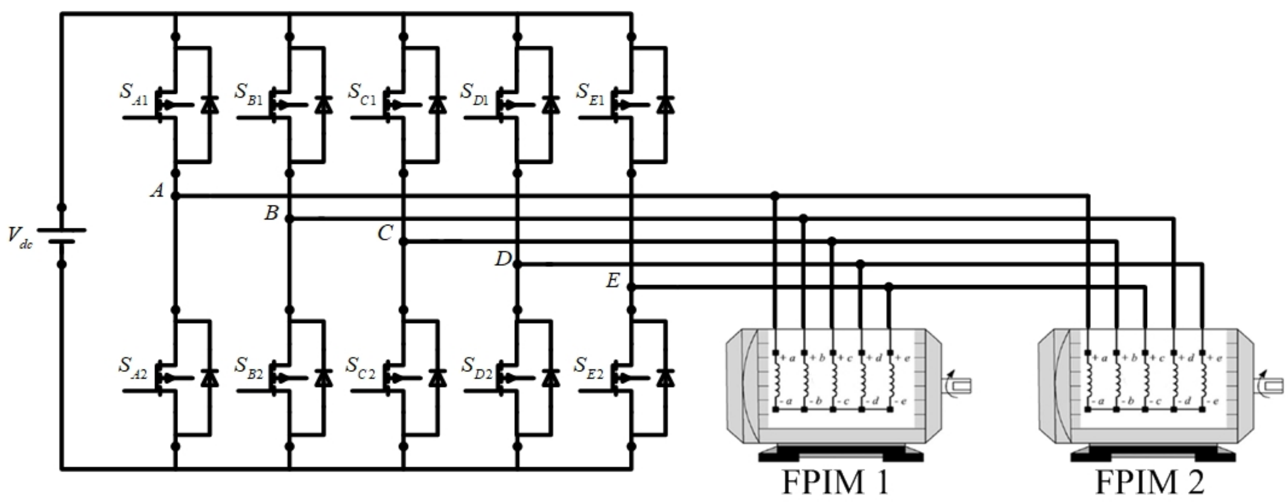

Figure 1. Two-motor drive schematic.

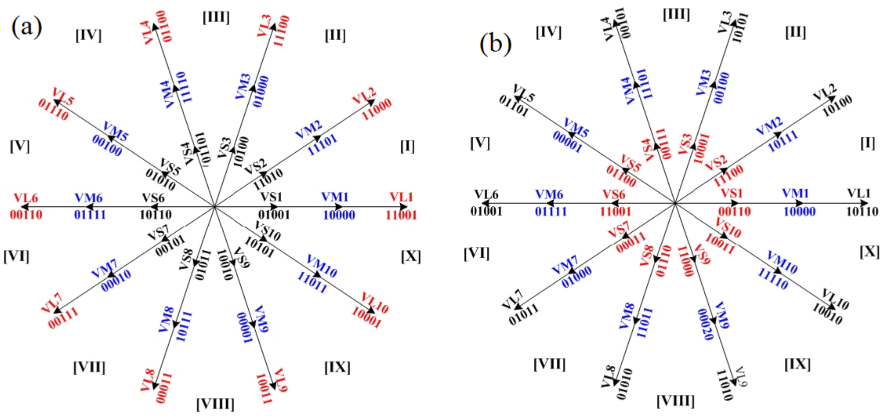

Figure 2. VVs switching sequences (a) VVs mapped in $\alpha\beta_1$ plane, (b) VVs mapped in $\alpha\beta_2$ plane.

[22, 23], is given by:

$$
\begin{cases}
v_{s1\alpha\beta_1} = R_{s1} i_{s1\alpha\beta_1} + L_{s1}\frac{di_{s1\alpha\beta_1}}{dt} + L_{m1}\frac{di_{r1}}{dt} = \\
\qquad R_{s2} i_{s2\alpha\beta_2} + L_{s2}\frac{di_{s2\alpha\beta_2}}{dt} \\
v_{s2\alpha\beta_2} = R_{s2} i_{s2\alpha\beta_2} + L_{s2}\frac{di_{s2\alpha\beta_2}}{dt} + L_{m2}\frac{di_{r2}}{dt} = \\
\qquad R_{s1} i_{s1\alpha\beta_1} + L_{s1}\frac{di_{s1\alpha\beta_1}}{dt} \\
0 = R_{rj} i_{rj} + L_{rj}\frac{di_{rj}}{dt} + L_{mj}\frac{di_{sj\alpha\beta j}}{dt} - j\omega_{rj}(L_{mj} i_{sj\alpha\beta j} + L_{rj} i_{rlj})
\end{cases}
\tag{4}
$$

The mechanical and electromagnetic torque expressions are given as follows:

$$
\begin{cases}
J_i \frac{d\omega_{mj}}{dt} = T_{emj} - T_{Lj} - f_j \omega_{mj} \\
T_{emj} = \frac{5p_j}{2}(\phi_{sj\alpha j} i_{sj\beta j} - \phi_{sj\beta j} i_{sj\alpha j})
\end{cases}
\tag{5}
$$

where: $j = 1$ or 2, $V_{sj\alpha\beta j}$ stator voltages, $i_{sj\alpha\beta j}$ stator currents, $\phi_{s\alpha}$, $\phi_{s\beta}$ stator flux linkages, i_r, rotor currents, R_s stator resistance, L_s stator leakage inductance, L_m mutual inductance, R_r rotor resistance, L_r rotor leakage inductance, ω_r rotor electrical speed, ω_m rotor mechanical speed, T_m electromagnetic torque, T_l load torque, p pair poles, j moment of inertia, f viscous friction coefficient.

3. The two FPIMS model

Figure 3 gives a representation of the two-level DTC for two parallel-connected FPIMs. In DTC, the flux orientation is determined through the instantaneous magnitude of the applied VV established on the processed error between the electromagnetic torque and stator flux actual and reference values through the seven-level and two-level HCs, respectively, in addition to the stator flux position using a predefined look-up table, Table 1 [23]. Following four basic steps:

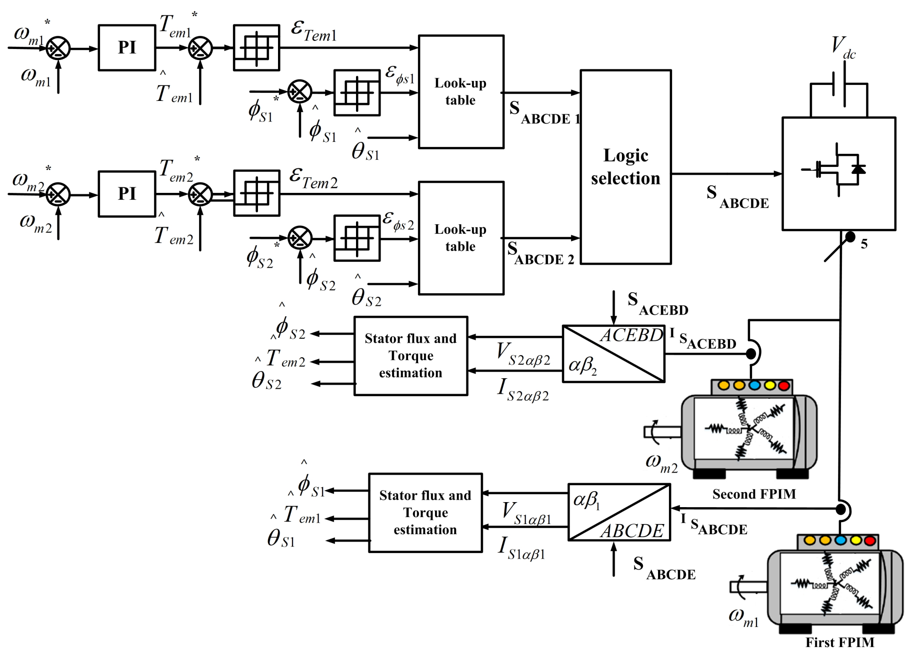

Figure 3. Schematic diagram of DTC for a two-motor drive.

3.1 Step one

The estimation of the stator flux vector and position and electromagnetic torque are based on the open-loop estimator expressed in Eq. (6) as follows:

$$\begin{cases} \hat{\phi}_{sj\alpha\beta j} = \int (v_{sj\alpha\beta j} - R_{sj} i_{sj\alpha\beta j}) dt \\ \hat{\phi}_{sj} = \sqrt{\hat{\phi}^2_{sj\alpha j} + \hat{\phi}^2_{sj\beta j}} \\ \hat{\theta}_{sj} = \tan^{-1}\left(\frac{\hat{\phi}_{sj\beta j}}{\hat{\phi}_{sj\alpha j}}\right) \\ \hat{T}_{emj} = \frac{5p_j}{2}(\hat{\phi}_{sj\alpha j} i_{sj\beta j} - \hat{\phi}_{sj\beta j} i_{sj\alpha j}) \end{cases} \tag{6}$$

3.2 Step two

The required actions on the stator flux and electromagnetic torque, either increasing or decreasing, are determined based on the digital response of the two-level and seven–level HCs for the stator flux and electromagnetic torque to the error between the reference and actual values as described in Eqs. (7) and (8), respectively. Figure 4 shows the structure of the two HCs.

$$\begin{cases} \mathrm{HB}_{\phi s1} >= \phi^*_{sj} - \hat{\phi}_{sj} & \varepsilon_{\phi sj} = 1 \\ -\mathrm{HB}_{\phi s1} <= \phi^*_{sj} - \hat{\phi}_{sj} & \varepsilon_{\phi sj} = -1 \end{cases} \tag{7}$$

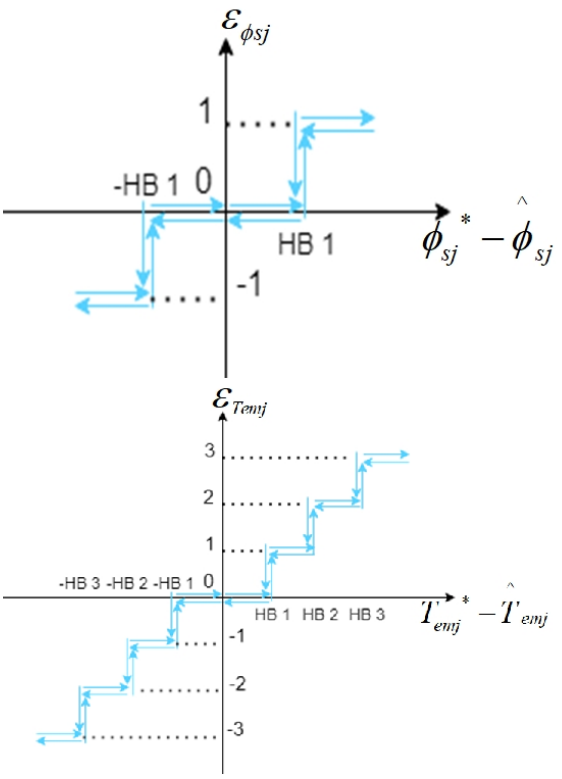

Figure 4. Structure of HCs: (a) Two-level HC, (b) Seven-level HC.

where: $\mathrm{HB}_{\phi s1}$ is the hysteresis band for the stator flux.

$$\begin{cases} \mathrm{HB}_{Tem3} > T^*_{emj} - \hat{T}_{emj} & \varepsilon_{Temj} = 3 \\ \mathrm{HB}_{Tem2} < T^*_{emj} - \hat{T}_{emj} <= \mathrm{HB}_{Tem3} & \varepsilon_{Temj} = 2 \\ \mathrm{HB}_{Tem1} < T^*_{emj} - \hat{T}_{emj} <= \mathrm{HB}_{Tem2} & \varepsilon_{Temj} = 1 \\ -\mathrm{HB}_{Tem1} < T^*_{emj} - \hat{T}_{emj} <= \mathrm{HB}_{Tem1} & \varepsilon_{Temj} = 0 \\ -\mathrm{HB}_{Tem2} < T^*_{emj} - \hat{T}_{emj} <= -\mathrm{HB}_{Tem1} & \varepsilon_{Temj} = -1 \\ -\mathrm{HB}_{Tem3} < T^*_{emj} - \hat{T}_{emj} <= -\mathrm{HB}_{Tem2} & \varepsilon_{Temj} = -2 \\ -\mathrm{HB}_{Tem3} <= T^*_{emj} - \hat{T}_{emj} & \varepsilon_{Temj} = -3 \end{cases} \tag{8}$$

where: $\pm\mathrm{HB}_{Tem1,\,2\text{ and }3}$ are the hysteresis bands for the electromagnetic torque.

3.3 Switching table

The two-motor drive requires the implementation of two distinct DTC controllers for independent control of each motor. Besides the phase transposition indicated in Figure 1, the control of the FPIM1 is developed in the $\alpha\beta_1$ plane and $\alpha\beta_2$ for the second motor. So, the resulting current components are flux/torque generating for one motor and non-generating for the other [21].

i.e., assuming that the flux of the first FPIM must be decreased ($\varepsilon_{\phi sj} = -1$), torque to be increased ($\varepsilon_{Temj} = 1$), while the stator flux lies in sector V, the selected VV from Table 2 is VS9 with a sequence of 10010 according to Figure 2 (a). Furthermore, if the flux module of FPIM2 lies in sector X and the torque and flux need to increased ($\varepsilon_{\phi sj} = 1$, $\varepsilon_{Temj} = 3$) the applied VV is VL1 with a sequence of 10110 from Figure 2 (b). The employed look-up table is given in Table 2.

3.4 Step four

The logic selection block permits alternatively applying the two control commands, VV, in every sampling period, e.g., the VV VS9 shall be applied for one period. Afterwards, the VV VL1 will be applied in the next period. Figure 5 depicts the schematic of the logic selection block.

Table 2. Look-up table for FPIM.

ε_{Temj}	$\varepsilon_{\phi sj}$	
	-1	1
3	VL$(i+4)$	VL$(i+1)$
2	VM$(i+4)$	VM$(i+1)$
1	VS$(i+4)$	VS$(i+1)$
0	V0	V0
-1	VS$(i+6)$	VS$(i+9)$
-2	VM$(i+6)$	VM$(i+9)$
-3	VL$(i+6)$	VL$(i+9)$

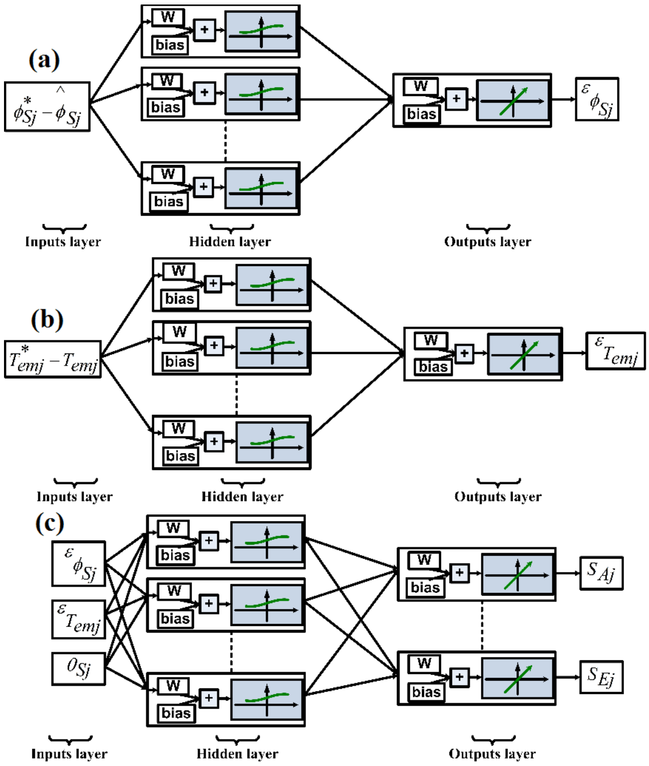

Figure 5. Structure of the implemented ANN controllers: (a) $HC_{\phi s}$−ANN, (b) HC_{Tem}−ANN, (c) ST−ANN.

4. Artificial neural network-based TORQUE direct control

A feed-forward back-propagation neural network controller is a universal approximator of complex functions. In our study case, the ANN is used to imitate the DTC working principle of the two HCs and the look-up table; in other words, it calculates the digital response corresponding to the errors between the flux and torque actual and reference values, as well as, determine the applied VV [6–8]. The ANN controller's structures are shown in Figure 5.
Figure 6 depicts the training process of the three ANN controllers, located parallel to the conventional scheme controllers to be imitated.
At first, random weights are applied to initiate the training process, resulting in a significant mismatch between the desired and calculated outputs for a given input. The error between the output patterns is used in the back-propagation algorithm to adjust the weights of the controllers. This procedure is carried on until the error of output patterns is minimized.
Table 3 summarizes the three ANN controllers' characteristics and structure.
As stated above, the SMO treated later accurately estimates the critical quantities, stator flux, and electromagnetic torque. The schematic of the drive is given in Figure 7.

5. Sliding mode observer

During the drive's low-speed operation, the DTC scheme's open-loop estimator experiences remarkable integration problems affecting the accuracy of the estimation process due to the initial value and DC-drift problems [20]. Therefore, a sliding mode observer is designed to reconstruct the FPIM state variables based on the switching sequence of the inverter and the measured currents [24].
This approach ensures a high dynamic performance and robustness over the entire speed range operation.
Figure 8 illustrates the schematics of SMO.
The SMO expression for the stator currents and flux estimation along the $\alpha\beta_j$ plane, based on the mathematical model

Table 3. Characteristic details of the proposed ANN controllers.

Controller parameters	Details		
	$HC_{\phi s} - ANN$	$HC_{Tem} - ANN$	$ST - ANN$
ANN type	Feed-forward BACKPROPAGATION neural network		
Learning algorithm	Levenberg Marquardt		
Activation function	Logsig	Logsig	Logsig
Learning rate	0.5	0.5	0.5
Input layer	1	1	3
Hidden layer	10	17	25
Output layer	1	1	5
Learning data	The learning process is based on collected data from the DTC method.		

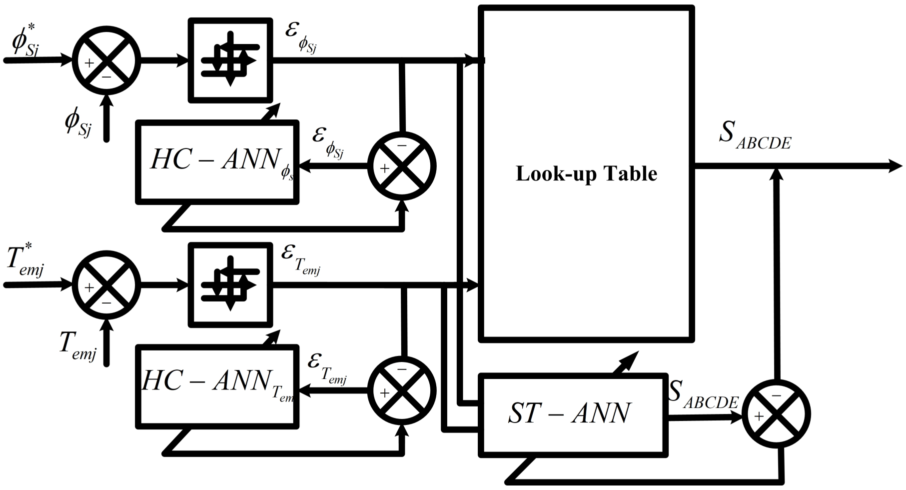

Figure 6. The training process of ANN controllers.

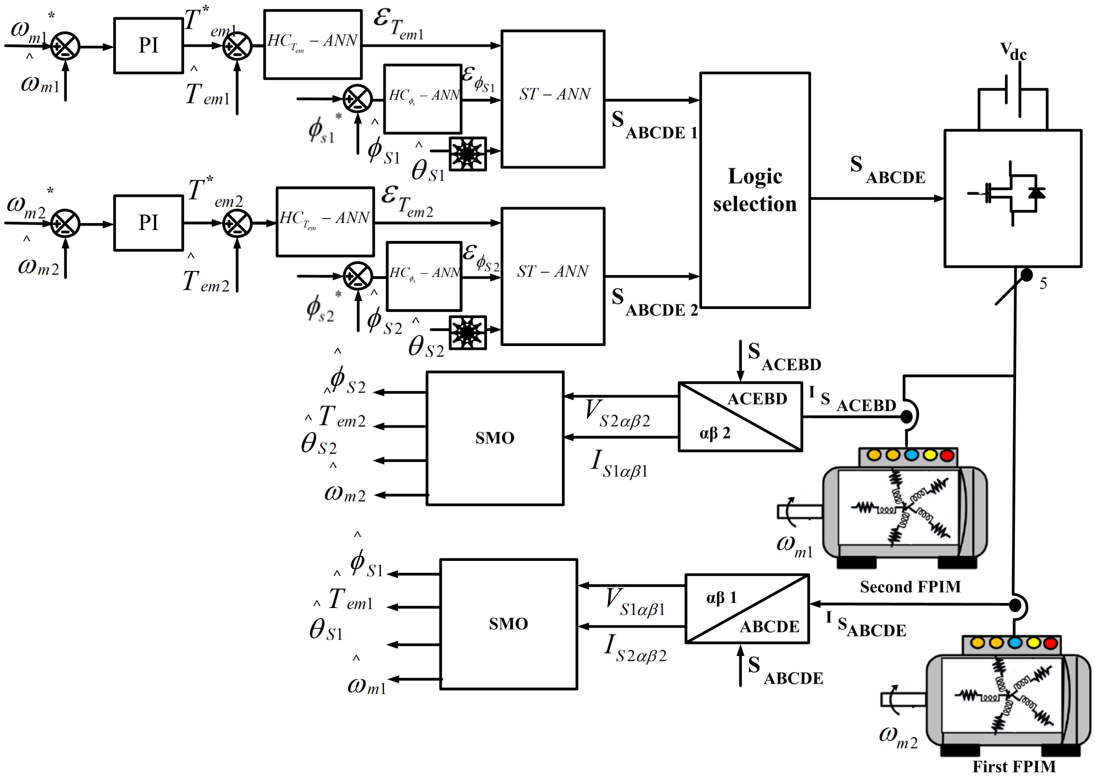

Figure 7. Schematic diagram of DTC-ANN for a two-motor drive.

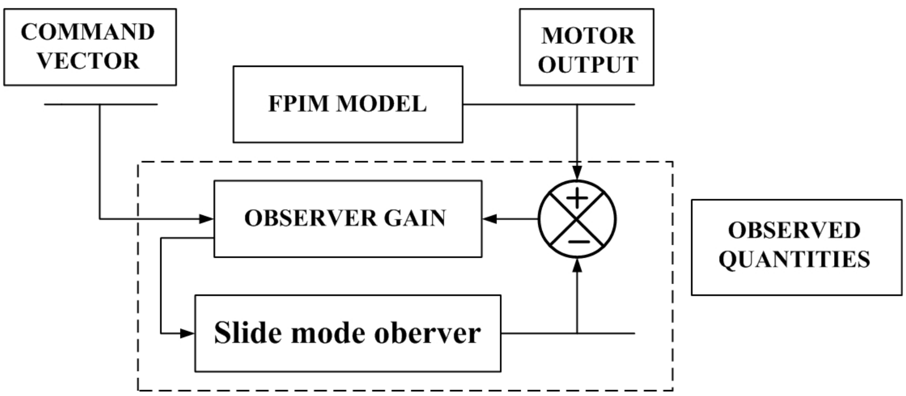

Figure 8. SMO schematic.

of the FPIM, is given as [24]:

$$\begin{cases} \frac{d\hat{i}_{s\alpha j}}{dt} = a_1\hat{i}_{s\alpha j} + a_6\hat{i}_{s\beta j} + a_2\hat{\phi}_{s\alpha j} + a_3\hat{\phi}_{s\beta j} + b_1 V_{s\alpha j} + \\ \qquad\qquad A_{i1}I_{s1} + A_{i2}I_{s2} \\ \frac{d\hat{i}_{s\beta j}}{dt} = -a_6\hat{i}_{s\alpha j} + a_1\hat{i}_{s\beta j} + a_3\hat{\phi}_{s\alpha j} + a_2\hat{\phi}_{s\beta j} + b_1 V_{s\beta j} + \\ \qquad\qquad A_{i3}I_{s1} + A_{i4}I_{s2} \\ \frac{d\hat{\phi}_{s\alpha j}}{dt} = a_4\hat{i}_{s\alpha j} + V_{s\alpha j} + A_{\phi 1}I_{s1} + A_{\phi 2}I_{s2} \\ \frac{d\hat{\phi}_{s\beta j}}{dt} = a_4\hat{i}_{s\beta j} + V_{s\beta j} + A_{\phi 3}I_{s1} + A_{\phi 4}I_{s2} \end{cases} \tag{9}$$

with

$$a_1 = -\left(\frac{R_{sj}+R_{rj}}{\sigma_j L_{sj}}\right) \qquad a_2 = \frac{R_{rj}}{\sigma_j L_{sj} L_{rj}}$$
$$a_3 = \frac{\omega_{rj}}{\sigma_j L_{sj}} \qquad a_4 = -R_{sj}$$
$$a_6 = -\hat{\omega}_{rj} \qquad b_1 = \frac{1}{\sigma_j L_{sj}}$$

where: $\hat{\phi}_{s\alpha j}$, $\hat{\phi}_{s\beta j}$, $\hat{i}_{s\alpha j}$ and $\hat{i}_{s\beta j}$ are the observed states of the FPIM: the stator flux and currents, respectively, in the stationary reference frame.

$$I_s = \begin{bmatrix} I_{s1} \\ I_{s2} \end{bmatrix} = \begin{bmatrix} \text{sign}(S1) \\ \text{sign}(S2) \end{bmatrix} \tag{10}$$

where

$$\begin{cases} S_1 = i_{s\alpha j} - \hat{i}_{s\alpha j} \\ S_2 = i_{s\beta j} - \hat{i}_{s\beta j} \end{cases} \tag{11}$$

and

$$I_{sj} = \begin{cases} 1, & \text{if } Sj >= 0 \\ -1, & \text{if } Sj < 0. \end{cases} \tag{12}$$

$A_{ix}(x = 1, 2, 3, 4)$ and $A_{\phi x}(x = 1, 2, 3, 4)$ are the SMO gains, and $S1$, $S2$, I_{s1}, and I_{s2} are the chosen sliding surfaces, and their signs, respectively.
The stator current and flux gain matrixes are written as follows:

$$\begin{bmatrix} A_{1i} & A_{2i} \\ A_{1i} & A_{2i} \end{bmatrix} = D \begin{bmatrix} \delta_1 & 0 \\ 0 & \delta_2 \end{bmatrix} \tag{13}$$

$$\begin{bmatrix} A_{\phi 1} & A_{\phi 2} \\ A_{\phi 1} & A_{\phi 2} \end{bmatrix} = \begin{bmatrix} \left(q_1 - \frac{R_{rj}}{L_{rj}}\right)\delta_1 & \frac{\hat{\omega}_{rj}}{\sigma_j L_{sj}} \\ \frac{-\hat{\omega}_{rj}}{\sigma_j L_{sj}} & \left(q_1 - \frac{R_{rj}}{L_{rj}}\right)\delta_2 \end{bmatrix} \tag{14}$$

with

$$D = \begin{bmatrix} \frac{R_{rj}}{\sigma_j L_{sj} L_{rj}} & \frac{\hat{\omega}_{rj}}{\sigma_j L_{sj}} \\ \frac{-\hat{\omega}_{rj}}{\sigma_j L_{sj}} & \frac{R_{rj}}{\sigma_j L_{sj} L_{rj}} \end{bmatrix}$$

δ_1, δ_2, q_1, and q_2 are positive constants to be determined per Lyapunov's stability condition. The observer stability depends on the convergence of the observed stator current toward the sliding surface through the optimum determination of δ_1 and δ_2. The function candidate is [18, 25]:

$$V = \frac{1}{2} S^T S \tag{15}$$

To ensure the convergence of the system around the sliding surface S, the observation error of the stator current should be zero. Thus, the derivative function of Lyapunov must be forced to be strictly negative.

$$V = \frac{1}{2} S^T S < 0 \tag{16}$$

Thereby, the stability condition holds true if and only if the inequality (11) is satisfied:

$$\begin{cases} \delta_1 \geq |\varepsilon_{\phi\alpha}| \\ \delta_2 \geq |\varepsilon_{\phi\beta}| \end{cases} \tag{17}$$

The stator flux vector and position, as well as the electromagnetic torque, are estimated as follows:

$$\begin{cases} \hat{\phi}_{sj} = \sqrt{\hat{\phi}^2_{s\alpha j} + \hat{\phi}^2_{s\beta j}} \\ \theta_{sj} = \tan^{-1}\left(\frac{\hat{\phi}_{s\beta j}}{\hat{\phi}_{s\alpha j}}\right) \\ \hat{T}_{emj} = \frac{5p_j}{2}(\hat{\phi}_{s\alpha j} i_{s\beta j} - \hat{\phi}_{s\beta j} i_{s\alpha j}) \end{cases} \tag{18}$$

As for the rotor speed and electromagnetic torque estimation, their expressions are given as follows:

$$\begin{cases} \frac{d\hat{\omega}_{mjj}}{dt} = \frac{1}{J_i}(p_i(\hat{\phi}_{s\alpha j} i_{s\beta j} - \hat{\phi}_{s\beta j} i_{s\alpha j}) - \hat{T}_{Li} - f_j\hat{\omega}_{mj}) \\ \hat{T}_{emj} = p_i(\hat{\phi}_{s\alpha j} i_{s\beta j} - \hat{\phi}_{s\beta j} i_{s\alpha j}) \end{cases} \tag{19}$$

6. Load torque estimator

The load torque is an essential parameter for an accurate speed estimation, enhancing the control technique performance. Therefore, an estimation of the load torque is suggested utilizing stator flux and rotor mechanical speed.
The estimator equation is derived from the mechanical equation of the FPIM, using the estimated stator flux and rotor speed providing an online estimation, as follows [26]:

$$\hat{T}_{Li} = p_i(\hat{\phi}_{s\alpha j} i_{s\beta j} - \hat{\phi}_{s\beta j} i_{s\alpha j}) - J_i \frac{d\hat{\omega}_{mjj}}{dt} - f_j\hat{\omega}_{mj} \tag{20}$$

The structure of the load torque estimation is depicted in Figure 9.

7. Simulation results

Two tests are undertaken for several operation scenarios to evaluate the described DTC-ANN scheme's performance. The simulation results are presented and described herein. The two FPIM parameters are detailed in Table 4.

7.1 First test

This test exercises a constant load torque on both motors of 8 Nm. The speed reference commands undergo several variations from low to high-speed operation and speed reversion. Tables 5 and 6 summarize the first test scenario. The simulation results, low and reversion speed test, are shown in Figures 10 to 15.

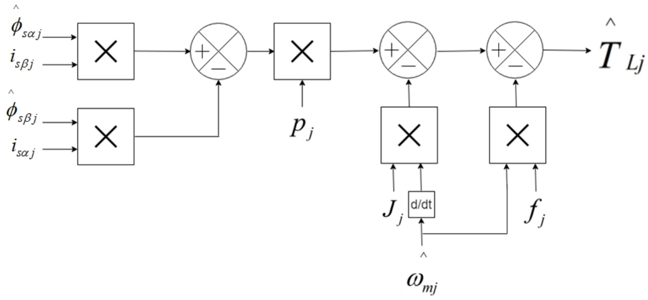

Figure 9. Load torque estimator.

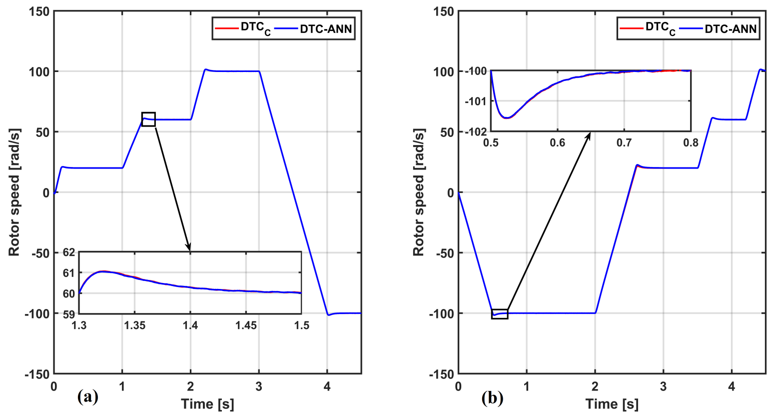

Figure 10. The rotor speed response: (a) FPIM1, (b) FPIM2.

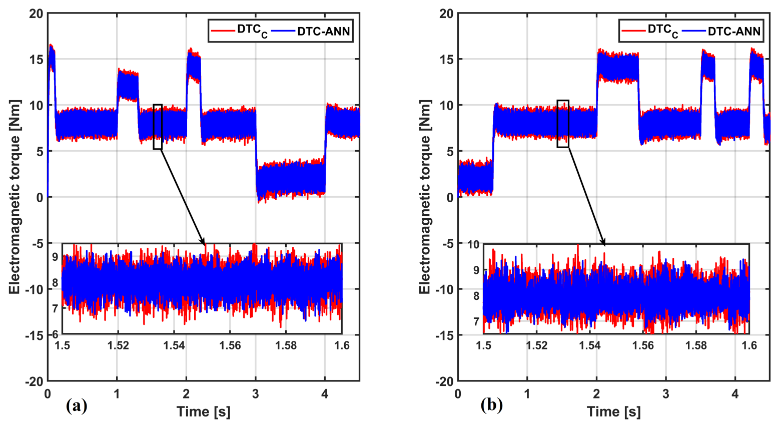

Figure 11. The electromagnetic torque response: (a) FPIM1, (b) FPIM2.

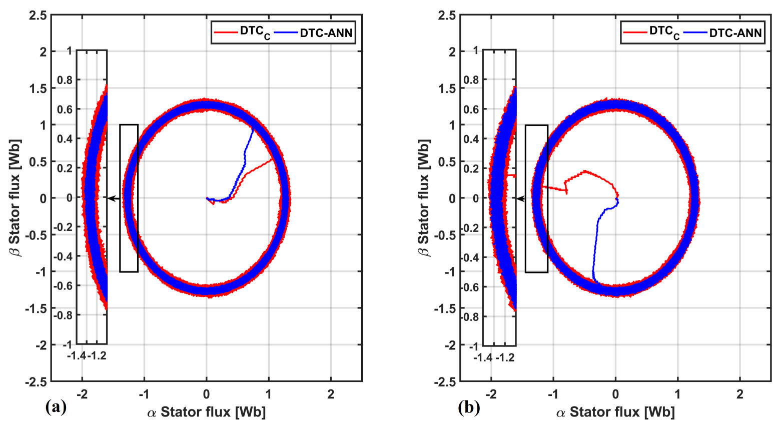

Figure 12. The stator flux response: (a) FPIM1, (b) FPIM2.

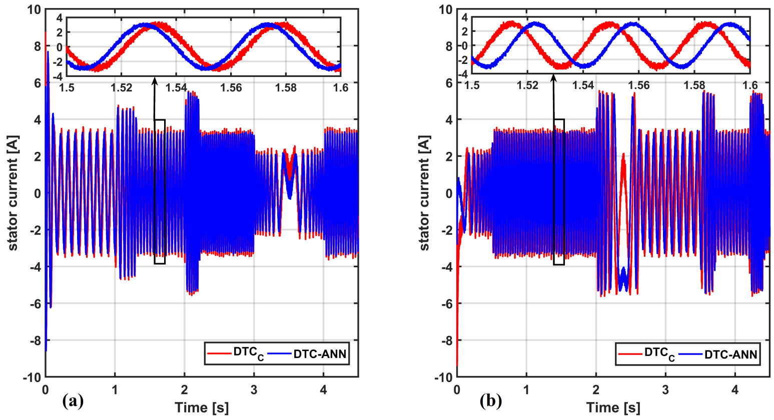

Figure 13. Phase “a” stator current: (a) FPIM1, (b) FPIM2.

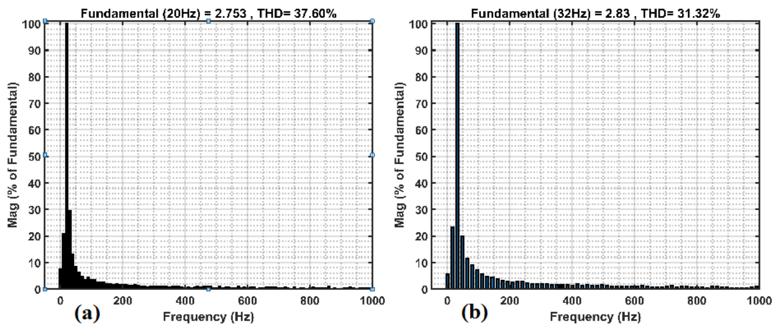

Figure 14. Phase “a” stator current THD analysis for DTC method: (a) FPIM1, (b) FPIM2.

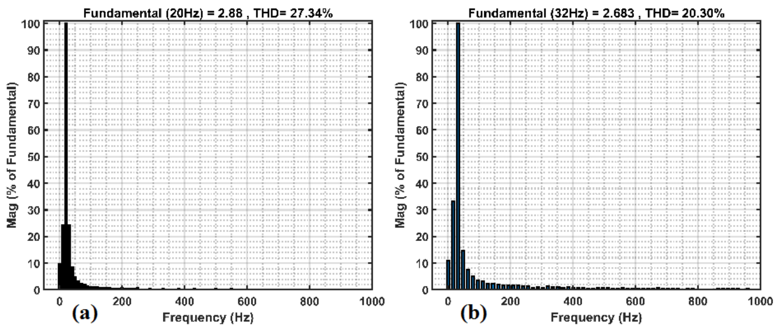

Figure 15. Phase “a” stator current THD analysis for DTC-ANN method: (a) FPIM1, (b) FPIM2.

7.2 Second test

For this test, both motors run at a constant speed of 100 rad/s. A step variation of the load torque is introduced on both motors. Table 7 summarizes the first test scenario.
The simulation results for step variation of load the torque test are shown in figures 16 to 21.

7.3 Discussion

The simulative results, figures 10, 11, 12, 13, 14, 15, 16, 17, 18, 19, 20, and 21, depict an independent control of the two-motor drive and a complete decoupling of the stator flux and electromagnetic torque despite the variation of the operating scenarios.
First, the actual, reference, and estimated rotor speed of the two motors are shown in Figures 10, 16, 20, and 21 for different loading conditions, in which it follows their reference commands with minimum over/undershot and a negligible error of ± 4 rad/s during the transient state and nearly null at steady state operation.
The electromagnetic torque response of the drive is depicted in Figures 11 and 17 for constant and step variation of the load torque. The present results clarify the efficiency of DTC-ANN in reducing the torque ripples by 20% compared to DTC.
The stator flux trajectories in the plane for the two motors are shown in Figures 12 and 18. The DTC-ANN improves the flux waveform in terms of fast response and less ripple content by 48% compared to DTC.
Furthermore, the phase “a” stator current waveform for both motors and the THD content is illustrated in Figures 13, 14, and 15, respectively. The stator current presents a better waveform and less current harmonic content by 10% in the case of DTC-ANN compared to DTC. This observation can be related to reducing the stator flux and electromagnetic

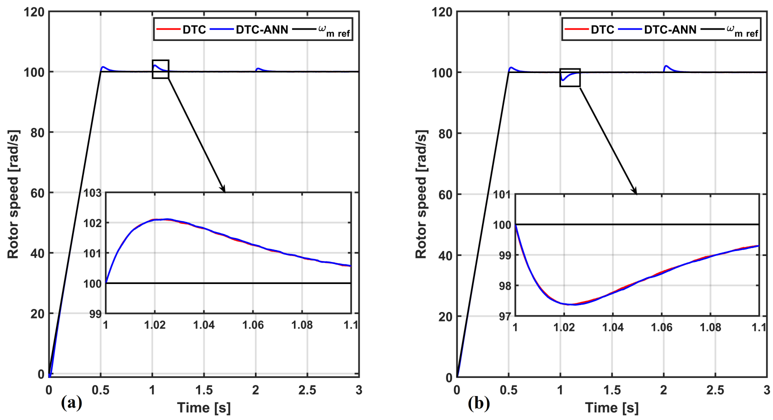

Figure 16. The rotor speed response: (a) FPIM1, (b) FPIM2.

Table 4. FPIM parameters.

1 Hp ; 200 V; 50 Hz; 1400 rpm	
R_s [Ω]	10
R_r [Ω]	6.3
L_s [Ω]	0.4642
L_r [Ω]	0.4612
L_m [H]	0.4212
J [Kg.m^2]	0.03
f [(Nm.s^{-1})/rad]	0.0001
T_{em} [N.m]	8
p	2

Table 5. First test scenario for the FPIM1.

Time [S]	ω_m [rad/s]	T_L [Nm]
$0 \to 0.1$	$0 \to 20$	8
$0.1 \to 1$	20	
$1 \to 1.3$	$20 \to 60$	
$1.3 \to 2$	60	
$2 \to 2.2$	$60 \to 100$	
$2.2 \to 3$	100	
$3 \to 4$	$100 \to -100$	
$4 \to 4.5$	-100	

torque ripples.
This reduction is due to a better selection of the optimum VV to be applied by ANN controllers, in addition to the accurate and robust estimation of the state variables of the two motors through the SMO. These improvements can be translated to the conformity of the state variables with their reference commands.

The estimated load torque is depicted in Figure 19, showing a precise estimation with negligible error of ± 0.4 Nm.

Table 6. First test scenario for the FPIM2.

Time [S]	ω_m [rad/s]	T_L [Nm]
$0 \to 0.5$	$0 \to -100$	8
$0.5 \to 2$	-100	
$2 \to 2.6$	$-100 \to 0$	
$2.6 \to 3.4$	20	
$3.4 \to 3.7$	$20 \to 60$	
$3.7 \to 4.2$	60	
$4.2 \to 4.4$	$60 \to 100$	
$4.4 \to 4.5$	100	

Table 7. Second test scenario for the two motors.

<table>
<tr><th>Time [S]</th><th>ω_m [rad/s]</th><th>T_{L1} [Nm]</th><th>T_{L2} [Nm]</th></tr>
<tr><td>$0 \to 0.5$</td><td>$0 \to -100$</td><td rowspan="2">8</td><td rowspan="2">-2</td></tr>
<tr><td>$0.5 \to 1$</td><td rowspan="2">100</td></tr>
<tr><td>$1 \to 2$</td><td>0</td><td>8</td></tr>
<tr><td>$2 \to 3$</td><td></td><td>-4</td><td>0</td></tr>
</table>

From the previous results, one can notice a full-decoupled control between the two machines' stator flux and electromagnetic torque regardless of the machine's operation mode, motoring, or generating mode. Therefore, the independent and stable operation of the parallel connected drive is ensured and investigated through the simulation results. Table 8. summarizes the simulation results through a comparative study of the two control schemes.

8. Conclusion

This study addresses the SMO-based sensorless DTC-ANN of two parallel-connected FPIM drives to circumvent two significant DTC problems. First, the ANN controllers are implemented to replace digital hysteresis controllers and look-up table, resulting in a reduction of the stator flux

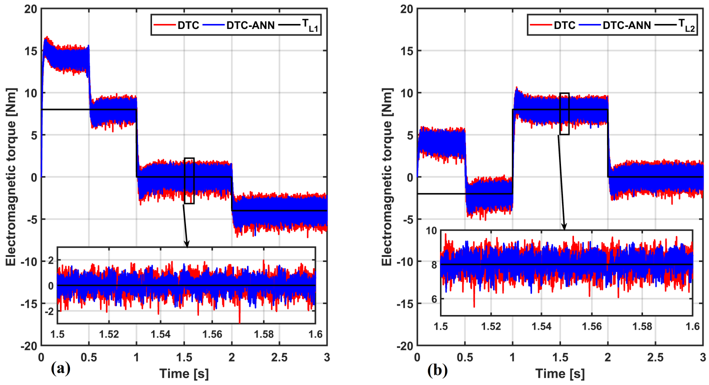

Figure 17. The electromagnetic torque response: (a) FPIM1, (b) FPIM2.

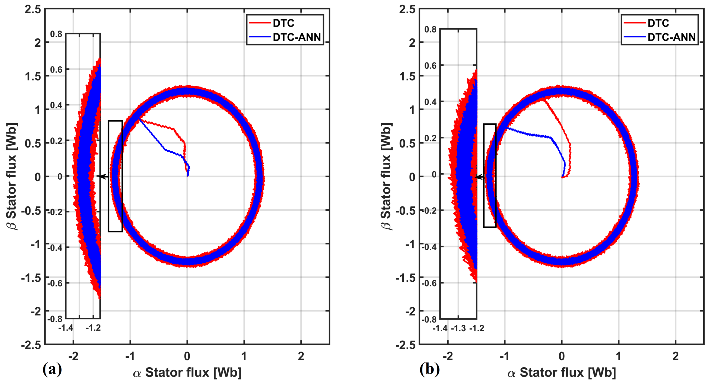

Figure 18. The stator flux response: (a) FPIM1, (b) FPIM2.

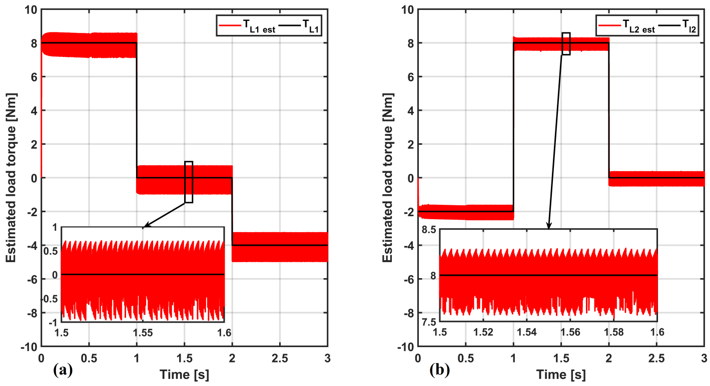

Figure 19. The estimated load torque: (a) FPIM1, (b) FPIM2.

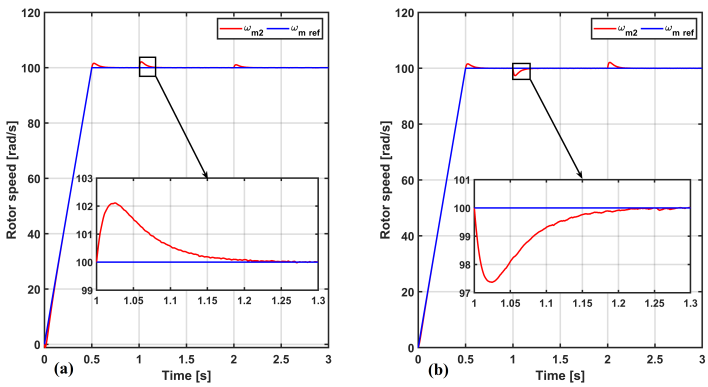

Figure 20. The estimated rotor speed: (a) FPIM1, (b) FPIM2.

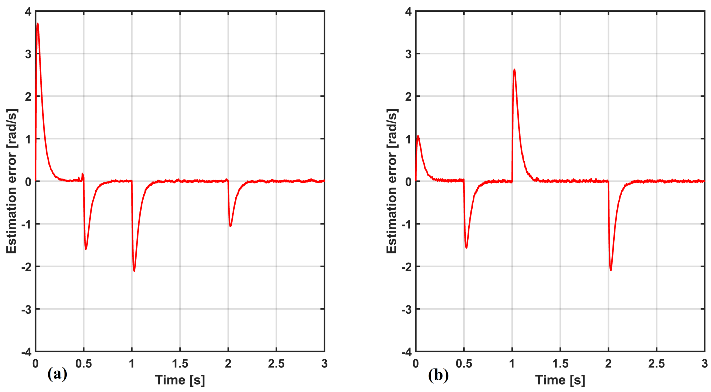

Figure 21. Estimation error of rotor speed: (a) FPIM1, (b) FPIM2.

Table 8. Comparative analysis of the performance of DTC and DTC-ANN.

Assessment parameters		FPIM1		FPIM1	
		DTC	DTC-ANN	DTC	DTC-ANN
ω_m	Recovery time (s)	0.3	0.3	0.3	0.3
	Overshoot (rad/s)	2	2	2	2
	Undershoot (rad/s)	2	2	2	2
	Estimation error (rad/s)	–	±3	–	±2
ϕ_s	Ripples (Wb)	0.1894	0.0988	0.1889	0.0986
T_{em}	Ripples (Nm)	3.6607	2.9917	3.4775	3.1329
T_L	Estimation error (Nm)	–	±0.4	–	±0.4
I_s	THD (%)	37.6	27.34	31.32	20.3

and torque ripples by 48% and 20%, respectively, which can be observed in an improvement of the quality of the current waveform through the reduction of THD by 10% compared to DTC. Second, the open-loop estimator affects the DTC scheme performance, especially during the low-speed region. Therefore, an SMO is introduced to address this problem, showing a high capability of tracking the FPIMs' state variables under different operating scenarios of speed and load torque variations with negligible error, which results in better selection of the optimal VV to be applied. Detailed simulations investigating the suggested method performance are presented.

Authors contributions
All authors have contributed equally to prepare the paper.

Availability of data and materials
The data that support the findings of this study are available from the corresponding author upon reasonable request.

Conflict of interests
The authors declare that they have no known competing financial interests or personal relationships that could have appeared to influence the work reported in this paper.

References

[1] M. Bermudez et al. “**An experimental assessment of open-phase fault-tolerant virtual-vector-based direct torque control in five-phase induction motor drives**.”. *IEEE Transactions on Power Electronics*, 33(3):pp. 2774–2784, 2018. DOI: https://doi.org/10.1109/tpel.2017.2711531.

[2] S. Guedida et al. “**Direct torque control scheme for less harmonic currents and torque ripples for dual star induction motor**.”. *Revue Roumaine des Sciences Techniques, Série Électrotechnique et Énergétique*, 68(4):pp. 331–338, 2023. DOI: https://doi.org/10.59277/RRST-EE.2023.4.2.

[3] E. Levi. “**Multiphase electric machines for variable-speed applications**.”. *IEEE Transactions on Industrial Electronics*, 55(5):pp. 1893–1909, 2008. DOI: https://doi.org/10.1109/tie.2008.918488.

[4] S. Payami, R. K. Behera, and A. Iqbal. “**DTC of three-level NPC inverter fed five-phase induction motor drive with novel neutral point voltage balancing scheme**.”. *IEEE Transactions on Power Electronics*, 33(2):pp. 1487–1500, 2018. DOI: https://doi.org/10.1109/tpel.2017.2675621.

[5] Y. N. Tatte and M. V. Aware. “**Torque ripple and harmonic current reduction in a three-level inverter-fed direct-torque-controlled five-phase induction motor**.”. *IEEE Transactions on Industrial Electronics*, 64(7):pp. 5265–5275, 2017. DOI: https://doi.org/10.1109/tie.2017.2677346.

[6] S. Mahfoud et al. “**Enhancement of the direct torque control by using artificial neuron network for a doubly fed induction motor**.”. *Intelligent Systems with Applications*, 13, 2022. DOI: https://doi.org/10.1016/j.iswa.2022.200060.

[7] S. Gdaim, A. Mtibaa, and M. F. Mimouni. “**Artificial Neural Network-based DTC of an induction machine with experimental implementation on FPGA**.”. *Engineering Applications of Artificial Intelligence*, 121:pp. 105972, 2023. DOI: https://doi.org/10.1016/j.engappai.2023.105972.

[8] A. Ghamri et al. “**Comparative study of ANN DTC and conventional DTC controlled PMSM Motor**.”. *Mathematics and Computers in Simulation*, 167:pp. 219–230, 2020. DOI: https://doi.org/10.1016/j.matcom.2019.09.006.

[9] R. Araria, K. Negadi, and F. Marignetti. “**Design and analysis of the speed and torque control of Im with DTC based Ann Strategy for Electric Vehicle Application**. ”. *TECNICA ITALIANA-Italian Journal of Engineering Science*, 63(2-4):pp. 181–188, 2019. DOI: https://doi.org/10.18280/ti-ijes.632-410.

[10] H. Benbouhenni. “**Seven-level direct torque control of induction motor based on artificial neural networks with regulation speed using fuzzy PI controller**.”. *Iranian Journal of Electrical and Electronic Engineering*, 14(1):pp. 85–94, 2018. DOI: https://doi.org/10.22068/IJEEE.14.1.85.

[11] R. Kumar et al. “**Artificial neural network based direct torque control of induction motor drives**.”. *IET-UK International Conference on Information and Communication Technology in Electrical Sciences (ICTES)*, :361–367, 2007. DOI: https://doi.org/10.1049/ic:20070638.

[12] A. Zemmit, S. Messalti, and A. Harrag. “**Innovative improved Direct Torque Control of Doubly Fed Induction Machine (DFIM) using Artificial Neural Network (ANN-DTC)**.”. *International Journal of Applied Engineering Research*, 11(16):pp. 9099–9105, 2016.

[13] Y. N. Tatte et al. “**Performance improvement of three-level five-phase inverter-fed DTC-controlled five-phase induction motor during low-speed operation**.”. *IEEE Transactions on Industry Applications*, 54(3):pp. 2349–2357, 2018. DOI: https://doi.org/10.1109/tia.2018.2798593.

[14] R. Inan. “**A novel fpga-based BI input-reduced order extended Kalman filter for speed-sensorless direct torque control of induction motor with constant switching frequency controller**.”. *IET Computers & amp; Digital Techniques*, 15(3):pp. 185–201, 2021. DOI: https://doi.org/10.1049/cdt2.12011.

[15] T. Kamel et al. “**Extended Kalman filter based sliding mode control of parallel-connected two five-phase PMSM Drive System**.”. *Electronics*, 7(2):pp. 14, 2018. URL 10.3390/electronics7020014.

[16] E. Zerdali and M. Barut. “**Extended Kalman filter based speed-sensorless load torque and inertia estimations with observability analysis for Induction Motors**.”. *Power Electronics and Drives*, 3(1):pp. 115–127, 2018. DOI: https://doi.org/10.2478/pead-2018-0002.

[17] S. Guedida et al. “**Novel speed sensorless DTC design for a five-phase induction motor with an intelligent fractional order controller based-mras estimator**.”. *Power Electronics and Drives*, 9(1):pp. 63–85, 2024. DOI: https://doi.org/10.2478/pead-2024-0005.

[18] S. Jnayah and A. Khedher. “**Sensorless direct torque control of induction motor using Sliding mode flux observer**.”. *19th International Conference on Sciences and Techniques of Automatic Control and Computer Engineering (STA)*, page pp. 536–541, 2019. DOI: https://doi.org/10.1109/sta.2019.8717270.

[19] Y. Zhang et al. “**A comparative study of Luenberger Observer, sliding mode observer and extended Kalman filter for sensorless vector control of induction motor drives**.”. *IEEE Energy Conversion Congress and Exposition*, page pp. 2466–2473, 2009. DOI: https://doi.org/10.1109/ecce.2009.5316508.

[20] A. Ammar, A. Bourek, and A. Benakcha. "**Sensorless SVM-direct torque control for Induction Motor Drive using sliding mode observers**.". *Journal of Control, Automation and Electrical Systems*, 28(2):pp. 189–202, 2016. DOI: https://doi.org/10.1007/s40313-016-0294-7.

[21] K. M. S. Benzaoui, E. Benyoussef, and A. Z. Kouache. "**Three-level direct torque control based on common mode voltage reduction strategy FED Two parallel connected Five-Phase induction machine**.". *Revue Roumaine DES Sciences Techniques-Série Électrotechnique et Énergétique*, 69(2):pp. 177–182, 2024. DOI: https://doi.org/10.59277/RRST-EE.2024.69.2.10.

[22] M. Bermudez et al. "**Open-phase fault-tolerant direct torque control technique for five-phase induction motor drives**.". *IEEE Transactions on Industrial Electronics*, 64(2):pp. 902–911, 2017. DOI: https://doi.org/10.1109/tie.2016.2610941.

[23] O. Saadeh, M. Dalbah, and Z. Dalala. "**Control of two five-phase parallel connected single source motor drives under balanced and unbalanced conditions**.". *9th IEEE International Symposium on Power Electronics for Distributed Generation Systems (PEDG)*, 2018. DOI: https://doi.org/10.1109/pedg.2018.8447807.

[24] A. Bıçak and A. Gelen. "**Sensorless Direct Torque Control based on seven-level torque hysteresis controller for five-phase IPMSM using a sliding-mode observer**.". *Engineering Science and Technology, an International Journal*, 24(5):pp. 1134–1143, 2021. DOI: https://doi.org/10.1016/j.jestch.2021.02.004.

[25] M. Ghanes. "**Observation et commande de la machine asynchrone sans capteur mécanique**.". *Thèse de doctorat*, 2005.

[26] F. Mehazzem. "**Contribution à la commande d'un moteur asynchrone destiné à la traction électrique**.". *Thèse de doctorat*, 2010.